First study of neutrino angle reconstruction using quasielasticlike interactions in MicroBooNE

P. Abratenko,[38] D. Andrade Aldana,[14] L. Arellano,[22] J. Asaadi,[37] A. Ashkenazi,[36] S. Balasubramanian,[12] B. Baller,[12] A. Barnard,[29] G. Barr,[29] D. Barrow,[29] J. Barrow,[26] V. Basque,[12] J. Bateman,[15,22] O. Benevides Rodrigues,[14] S. Berkman,[25] A. Bhat,[7] M. Bhattacharya,[12] M. Bishai,[3] A. Blake,[19] B. Bogart,[24] T. Bolton,[18] M. B. Brunetti,[17,40] L. Camilleri,[10] D. Caratelli,[4] F. Cavanna,[12] G. Cerati,[12] A. Chappell,[40] Y. Chen,[33] J. M. Conrad,[23] M. Convery,[33] L. Cooper-Troendle,[30] J. I. Crespo-Anadón,[6] R. Cross,[40] M. Del Tutto,[12] S. R. Dennis,[5] P. Detje,[5] R. Diurba,[2] Z. Djurcic,[1] K. Duffy,[29] S. Dytman,[30] B. Eberly,[35] P. Englezos,[32] A. Ereditato,[7,12] J. J. Evans,[22] C. Fang,[4] W. Foreman,[14,20] B. T. Fleming,[7] D. Franco,[7] A. P. Furmanski,[26] F. Gao,[4] D. Garcia-Gamez,[13] S. Gardiner,[12] G. Ge,[10] S. Gollapinni,[20] E. Gramellini,[22] P. Green,[29] H. Greenlee,[12] L. Gu,[19] W. Gu,[3] R. Guenette,[22] P. Guzowski,[22] L. Hagaman,[7] M. D. Handley,[5] O. Hen,[23] C. Hilgenberg,[26] G. A. Horton-Smith,[18] A. Hussain,[18] B. Irwin,[26] M. S. Ismail,[30] C. James,[12] X. Ji,[27] J. H. Jo,[3] R. A. Johnson,[8] D. Kalra,[10] G. Karagiorgi,[10] W. Ketchum,[12] M. Kirby,[3] T. Kobilarcik,[12] N. Lane,[15,22] J.-Y. Li,[11] Y. Li,[3] K. Lin,[32] B. R. Littlejohn,[14] L. Liu,[12] W. C. Louis,[20] X. Luo,[4] P. Machado,[12] T. Mahmud,[19] C. Mariani,[39] J. Marshall,[40] N. Martinez,[18] D. A. Martinez Caicedo,[34] S. Martynenko,[3] A. Mastbaum,[32] I. Mawby,[19] N. McConkey,[31] L. Mellet,[25] J. Mendez,[21] J. Micallef,[23,38] A. Mogan,[9] T. Mohayai,[16] M. Mooney,[9] A. F. Moor,[5] C. D. Moore,[12] L. Mora Lepin,[22] M. M. Moudgalya,[22] S. Mulleriababu,[2] D. Naples,[30] A. Navrer-Agasson,[15] N. Nayak,[3] M. Nebot-Guinot,[11] C. Nguyen,[32] J. Nowak,[19] N. Oza,[10] O. Palamara,[12] N. Pallat,[26] V. Paolone,[30] A. Papadopoulou,[20] V. Papavassiliou,[28] H. B. Parkinson,[11] S. F. Pate,[28] N. Patel,[19] Z. Pavlovic,[12] E. Piasetzky,[36] K. Pletcher,[25] I. Pophale,[19] X. Qian,[3] J. L. Raaf,[12] V. Radeka,[3] A. Rafique,[1] M. Reggiani-Guzzo,[11] J. Rodriguez Rondon,[34] M. Rosenberg,[38] M. Ross-Lonergan,[20] I. Safa,[10] D. W. Schmitz,[7] A. Schukraft,[12] W. Seligman,[10] M. H. Shaevitz,[10] R. Sharankova,[12] J. Shi,[5] E. L. Snider,[12] S. Söldner-Rembold,[15] J. Spitz,[24] M. Stancari,[12] J. St. John,[12] T. Strauss,[12] A. M. Szelc,[11] N. Taniuchi,[5] K. Terao,[33] C. Thorpe,[22] D. Torbunov,[3] D. Totani,[4] M. Toups,[12] A. Trettin,[22] Y.-T. Tsai,[33] J. Tyler,[18] M. A. Uchida,[5] T. Usher,[33] B. Viren,[3] J. Wang,[27] M. Weber,[2] H. Wei,[21] A. J. White,[7] S. Wolbers,[12] T. Wongjirad,[38] K. Wresilo,[5] W. Wu,[30] E. Yandel,[4,20] T. Yang,[12] L. E. Yates,[12] H. W. Yu,[3] G. P. Zeller,[12] J. Zennamo,[12] and C. Zhang[3]

(MicroBooNE Collaboration)[*]

[1]*Argonne National Laboratory (ANL), Lemont, Illinois 60439, USA*
[2]*Universität Bern, Bern CH-3012, Switzerland*
[3]*Brookhaven National Laboratory (BNL), Upton, New York 11973, USA*
[4]*University of California, Santa Barbara, California 93106, USA*
[5]*University of Cambridge, Cambridge CB3 0HE, United Kingdom*
[6]*Centro de Investigaciones Energéticas, Medioambientales y Tecnológicas (CIEMAT), Madrid E-28040, Spain*
[7]*University of Chicago, Chicago, Illinois 60637, USA*
[8]*University of Cincinnati, Cincinnati, Ohio 45221, USA*
[9]*Colorado State University, Fort Collins, Colorado 80523, USA*
[10]*Columbia University, New York, New York 10027, USA*
[11]*University of Edinburgh, Edinburgh EH9 3FD, United Kingdom*
[12]*Fermi National Accelerator Laboratory (FNAL), Batavia, Illinois 60510, USA*
[13]*Universidad de Granada, Granada E-18071, Spain*
[14]*Illinois Institute of Technology (IIT), Chicago, Illinois 60616, USA*
[15]*Imperial College London, London SW7 2AZ, United Kingdom*
[16]*Indiana University, Bloomington, Indiana 47405, USA*
[17]*The University of Kansas, Lawrence, Kansas 66045, USA*
[18]*Kansas State University (KSU), Manhattan, Kansas 66506, USA*
[19]*Lancaster University, Lancaster LA1 4YW, United Kingdom*
[20]*Los Alamos National Laboratory (LANL), Los Alamos, New Mexico 87545, USA*
[21]*Louisiana State University, Baton Rouge, Louisiana 70803, USA*
[22]*The University of Manchester, Manchester M13 9PL, United Kingdom*
[23]*Massachusetts Institute of Technology (MIT), Cambridge, Massachusetts 02139, USA*
[24]*University of Michigan, Ann Arbor, Michigan 48109, USA*
[25]*Michigan State University, East Lansing, Michigan 48824, USA*
[26]*University of Minnesota, Minneapolis, Minnesota 55455, USA*
[27]*Nankai University, Nankai District, Tianjin 300071, China*

[28]*New Mexico State University (NMSU), Las Cruces, New Mexico 88003, USA*
[29]*University of Oxford, Oxford OX1 3RH, United Kingdom*
[30]*University of Pittsburgh, Pittsburgh, Pennsylvania 15260, USA*
[31]*Queen Mary University of London, London E1 4NS, United Kingdom*
[32]*Rutgers University, Piscataway, New Jersey 08854, USA*
[33]*SLAC National Accelerator Laboratory, Menlo Park, California 94025, USA*
[34]*South Dakota School of Mines and Technology (SDSMT), Rapid City, South Dakota 57701, USA*
[35]*University of Southern Maine, Portland, Maine 04104, USA*
[36]*Tel Aviv University, Tel Aviv, Israel, 69978*
[37]*University of Texas, Arlington, Texas 76019, USA*
[38]*Tufts University, Medford, Massachusetts 02155, USA*
[39]*Center for Neutrino Physics, Virginia Tech, Blacksburg, Virginia 24061, USA*
[40]*University of Warwick, Coventry CV4 7AL, United Kingdom*

(Received 24 April 2025; accepted 6 June 2025; published 27 June 2025)

We investigate the expected precision of the reconstructed neutrino direction using a ν_μ-argon quasielasticlike event topology with one muon and one proton in the final state and the reconstruction capabilities of the MicroBooNE liquid argon time projection chamber. This direction is of importance in the context of DUNE sub-GeV atmospheric oscillation studies. MicroBooNE allows for a data-driven quantification of this resolution by investigating the deviation of the reconstructed muon-proton system orientation with respect to the well-known direction of neutrinos originating from the Booster Neutrino Beam with an exposure of 1.3×10^{21} protons on target. Using simulation studies, we derive the expected sub-GeV DUNE atmospheric-neutrino reconstructed simulated spectrum by developing a reweighting scheme as a function of the true neutrino energy. We further report flux-integrated single- and double-differential cross section measurements of charged-current ν_μ quasielasticlike scattering on argon as a function of the muon-proton system angle using the full MicroBooNE data sets. We also demonstrate the sensitivity of these results to nuclear effects and final state hadronic reinteraction modeling.

DOI: 10.1103/f8nt-ygng

I. INTRODUCTION

Atmospheric neutrinos play a crucial role in improving our understanding of neutrino oscillations and extracting mixing parameters in the lepton sector, such as the charge-parity violating phase (δ_{CP}) [1,2]. Of particular interest are sub-GeV atmospheric neutrinos with energies in the 100 MeV to 1 GeV range. These are affected by both solar and atmospheric mass splittings, while being sensitive to nontrivial oscillation effects [3–6]. A measurement of their oscillation pattern can yield important new information on δ_{CP}. Furthermore, there are a wealth of phenomenological oscillation study efforts in this energy regime [7–23].

Atmospheric neutrinos' oscillatory nature will be extensively explored with precision measurements performed using data sets that will be collected, amongst others, by the forthcoming Deep Underground Neutrino Experiment (DUNE) [24–27]. The liquid argon time projection chamber (LArTPC) technology deployed by DUNE will be essential to that effort, since it enables excellent neutrino interaction topology and energy reconstruction by allowing the detection of the majority of the secondary charged particles with low detection thresholds for charged particles [28]. Yet, in addition to a good estimation of the neutrino energy, a precise reconstruction of the incoming neutrino direction and the accurate modeling of the nuclear effects are crucial to determine the event-by-event baseline necessary for studying oscillation effects and obtaining a measurement of δ_{CP} [23].

In this work, we investigate the precision of the reconstructed neutrino direction in a LArTPC detector using sub-GeV neutrinos arriving from a known direction. The reported results use the MicroBooNE detector [29] and data sets corresponding to an exposure of 1.3×10^{21} protons on target. Neutrinos from the Booster Neutrino Beam (BNB) [30] at Fermi National Accelerator Laboratory collected during 2015–2020 are used, which provide strong overlap with the sub-GeV atmospheric neutrino spectrum. We focus on interactions where a single muon-proton pair is reconstructed with no additional detected particles, similar to previous measurements [31–33]. We refer to these events as CC1p0π. Such events are dominated by quasielastic (QE) interactions as it is required that there are no visible pions.

*Contact author: microboone_info@fnal.gov

Published by the American Physical Society under the terms of the Creative Commons Attribution 4.0 International license. Further distribution of this work must maintain attribution to the author(s) and the published article's title, journal citation, and DOI. Funded by SCOAP³.

We define the direction of the muon-proton system from the sum of the muon and proton momentum, and investigate the deviation of this direction from that of the incoming neutrino. Furthermore, we present the first flux-integrated differential cross section measurements for muon-neutrino charged-current (CC) interactions on argon as a function of the angle between the muon-proton system and the incoming neutrino direction. We present both a single-differential measurement, and double-differential measurements in different ranges of variables with sensitivity to nuclear effects and undetected particles such as neutrons. These variables include the reconstructable energy, derived struck nucleon momentum, and derived missing momentum.

In Sec. II we define the angle between the muon-proton system and the incoming neutrino direction, θ_{vis}. We further define the variables with sensitivity to nuclear effects used in the double-differential cross section measurements. In Sec. III we present θ_{vis} distributions using MicroBooNE ν_μ-Ar CC1p0π interactions and discuss the observed features in specific regions of phase space. Section IV leverages the MicroBooNE CC1p0π event selection to make a projection for the expected DUNE atmospheric neutrino θ_{vis} spectrum by deriving a reweighting factor as a function of the true neutrino energy. In Sec. V we present the first flux-integrated single- and double-differential cross section measurements in the new angular variable. Finally, conclusions are presented in Sec. VI.

II. OBSERVABLES

The simplest case in which to benchmark the reconstructed neutrino angular orientation precision is using charged-current quasielasticlike (CCQE-like) interactions, where the final state can be characterized by a muon and a proton. Using the muon ($\vec{p}_\mu$) and proton ($\vec{p}_p$) momentum vectors, we define the angle between the muon-proton system and the incoming neutrino direction (θ_{vis}) as

$$\theta_{\text{vis}} = \text{acos}\left(\frac{\vec{b}\cdot\hat{z}}{|\vec{b}|}\right), \tag{1}$$

$$\text{with} \quad \vec{b} = \vec{p}_\mu + \vec{p}_p, \tag{2}$$

where $\hat{z}$ corresponds to the unit vector along the beam direction of incident neutrinos, as shown in Fig. 1.

This reconstructed angular orientation serves as a proxy for the neutrino direction and is studied as a function of variables with sensitivity to nuclear effects; namely the (i) visible energy, (ii) total struck nucleon momentum, and (iii) missing momentum.

The reconstructable visible energy (E_{reco}) is a crucial input to neutrino oscillation studies, and can be obtained following the formalism used in [34],

$$E_{\text{reco}} = E_\mu + K_p + B, \tag{3}$$

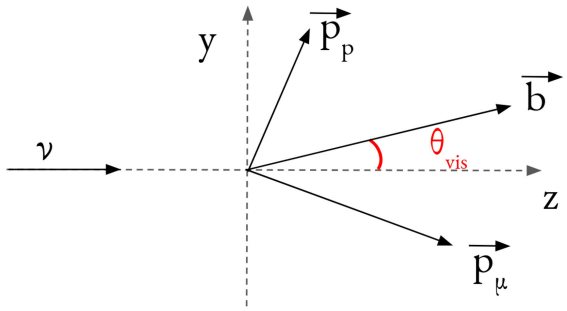


FIG. 1. Schematic representation of θ_{vis} using the muon's and proton's three-dimensional momentum vectors.

where E_μ is the total muon energy, K_p is the proton kinetic energy, and B the nucleon removal energy of argon set to 30.9 MeV [35]. The particle energies are obtained using range-based momentum.

Assuming that the incoming neutrino travels along the z-direction and using conservation of momentum along that direction, the transverse and longitudinal components of the struck nucleon momentum can be obtained, as discussed in Refs. [36,37],

$$\delta\vec{p}_T = \vec{p}_{\mu,T} + \vec{p}_{p,T}, \tag{4}$$

$$p_L = p_{\mu,L} + p_{p,L} - E_{\text{reco}}, \tag{5}$$

where $p_{\mu(p),T(L)}$ are the transverse (longitudinal) component of the muon (proton) momentum vector, respectively. Assuming that all the particles are reconstructed, the initial struck nucleon momentum (p_n) can be obtained as the vector sum of the longitudinal and transverse components,

$$p_n = |\vec{p}_n| = \sqrt{p_L^2 + \delta p_T^2}. \tag{6}$$

This derivation of the initial struck nucleon momentum builds on the assumption that neutrinos arrive from a known direction along the beamline. This is not applicable for neutrinos of atmospheric origin. To overcome this limitation, we introduce a new variable to quantify the missing momentum as

$$p_{\text{miss}} = E_{\text{reco}} - b, \tag{7}$$

where b corresponds to the magnitude of the vector $\vec{b}$. This quantity is independent of the incoming neutrino direction since it uses no angular information. Thus, it can be calculated for atmospheric neutrinos and leveraged to ensure that both the incoming atmospheric neutrino direction and energy will be reconstructed accurately. In the absence of undetected particles, detection thresholds, or nuclear effects, p_{miss} would be equal to the proton-neutron mass difference. Deviations from that value are indicative

of the presence of these effects and introduce missing energy or momentum in the measurement.

III. MICROBOONE EVENT SELECTION

The CC1p0π signal definition used in this analysis includes all ν_μ-Ar scattering events with a final-state muon with momentum $0.1 < p_\mu < 1.2$ GeV/c, and exactly one proton with $0.3 < p_p < 1$ GeV/c. Events with final-state neutral pions of any momentum are excluded. Signal events may contain any number of protons with momentum less than 300 MeV/c or greater than 1 GeV/c, neutrons of any momentum, and charged pions with momentum lower than 70 MeV/c.

To report the results as a function of the θ_{vis} angular orientation, we use five years of data collected by the MicroBooNE detector from its exposure to the BNB neutrino flux. The detector is an 85 tonne active mass liquid argon time projection chamber and is described in detail in Ref. [29].

The selection outlined in Refs. [31–33] is used, which corresponds to the same CC1p0π signal definition as described at the beginning of this section. This results in 17,130 candidate data events, a purity of CC1p0π interactions of about 70%, and a selection efficiency of approximately 10%. The final efficiency is primarily driven by the demand for exactly two fully contained tracklike candidates. Based on simulation predictions, we find that the dominant background contributions originate from events with two true protons, pion-proton pairs, and broken muon tracks. This is attributed to reconstruction failures that either fail to reconstruct a particle track or split a particle track into multiple segments.

This data is compared against the GENIEv3.0.6 neutrino interaction generator predictions [38] with the v3.0.6 `G18_10a_02_11a (G18)` model configuration along with the MicroBooNE BNB flux prediction [30]. This model configuration uses the local Fermi gas (LFG) model [39], the Nieves CCQE scattering prescription [40] which includes Coulomb corrections for the outgoing muon [41], and random phase approximation (RPA) corrections [42]. Additionally, it uses the Nieves meson exchange current (MEC) model [43], the Kuzmin-Lyubushkin-Naumov Berger-Sehgal resonance production (RES) [44–46], the Berger-Sehgal coherent production (COH) [47], and the Bodek-Yang deep inelastic scattering (DIS) [48] models with the PYTHIA [49] hadronization part, and the hA2018 final state interaction (FSI) model [50]. The CCQE and CCMEC neutrino interaction models have been tuned to T2K $\nu_\mu - {}^{12}$C CC0π data [51,52]. Predictions for more complex interactions, such as RES, remain unaltered and no additional Monte Carlo (MC) constraints are applied. We refer to the corresponding tuned prediction as `G18T`. In order to provide an accurate description of the dominant cosmic backgrounds pertinent to surface detectors, the full MC simulation consists of a combination of simulated neutrino interactions overlaid with background data collected when the beam is off to model cosmic ray induced interactions and detector noise. This technique has been extensively used by previous CC1p0π MicroBooNE analyses [53–56].

We first characterize the performance of the LArTPC reconstruction by comparing the true ($\vec{b}_{\text{true}}$) and reconstructed ($\vec{b}_{\text{reco}}$) muon-proton system vectors. These are constructed using the true and reconstructed values for the muon and proton momentum vectors, respectively, as defined in Sec. II. The true values refer to the MC generator-level quantities, while the reconstructed values refer to the quantities as measured in the LArTPC detector. This comparison is performed using the selected MC events that satisfy the CC1p0π signal definition. We refer to the relevant opening angle between the reconstructed (r) and true (t) $\vec{b}$ vectors as θ_{brt}, as shown in Fig. 2(a). As shown in Fig. 2(b), for the majority of events the angle θ_{brt} is better than 5°, which demonstrates the excellent reconstruction capabilities of LArTPCs. The peak location (p'), median (m), mean value (μ), and standard deviation ($\tilde{\sigma}$) describing the distributions are also shown. The small values that characterize this distribution indicate that the detector resolution on these quantities is not the limiting factor in determining the incoming neutrino direction. This will also be discussed in later sections. Finally, Fig. 2(c) shows the two-dimensional correlation between the reconstructed and true θ_{vis} and demonstrates that no major biases are observed. The corresponding muon and proton angular correlations between the reconstructed and true quantities can be found in the Supplemental Material [57].

The reconstructed θ_{vis} distribution is shown in Fig. 3. The uncertainty band shown in the data to MC ratio includes contributions from the neutrino flux prediction [58], neutrino interaction cross section modeling [52,59,60], detector response modeling [61], beam exposure, MC statistics, number of scattering targets, reinteractions [62], and out-of-cryostat interaction modeling. The data-simulation agreement is quantified across all the figures in terms of a goodness-of-fit metric (χ^2), the corresponding p-value (p), and as a number of standard deviations (σ'). The latter is calculated by translating the p-value to a χ^2 value with one degree of freedom and taking the square root of that quantity. The χ^2 calculation includes the bin-to-bin correlations.

In the absence of nuclear effects and final-state reinteractions, the θ_{vis} distribution would be peaked at 0° with respect to the incoming neutrino direction. Instead it shows a smooth rise at low values until it peaks at ≈10°, followed by a decreasing tail that extends to 180°. The physics contributions driving this tail are discussed in Sec. V. Candidate neutrino interactions that satisfy the CC1p0π signal definition at a reconstruction level but not at truth level are treated as background events. We refer to these

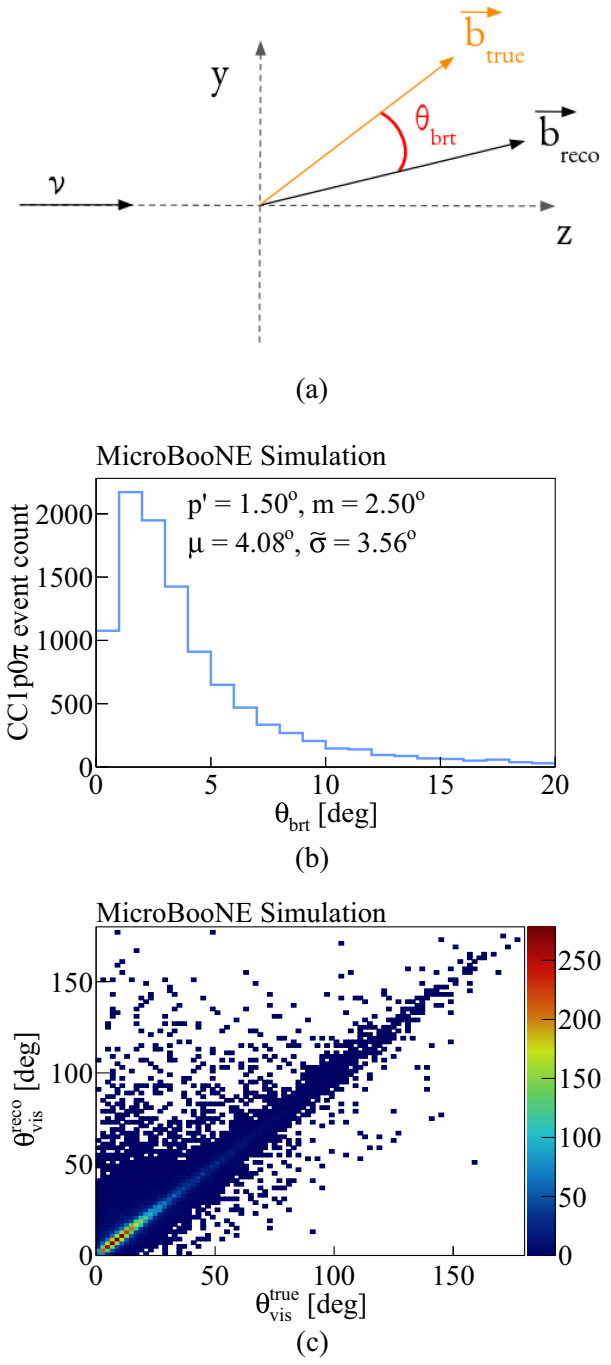


FIG. 2. (a) Schematic representation of the θ_{brt} angle using the angle between the true ($\vec{b}_{true}$) and reconstructed ($\vec{b}_{reco}$) muon-proton system vectors with respect to the neutrino orientation for selected signal CC1p0π simulated events. (b) Angular θ_{brt} distribution using the selected signal CC1p0π simulated events. The peak location (p'), median (m), mean value (μ), and standard deviation ($\tilde{\sigma}$) describing the distribution are also shown. (c) Two-dimensional correlation between the reconstructed and true θ_{vis} using the selected signal CC1p0π simulated events.

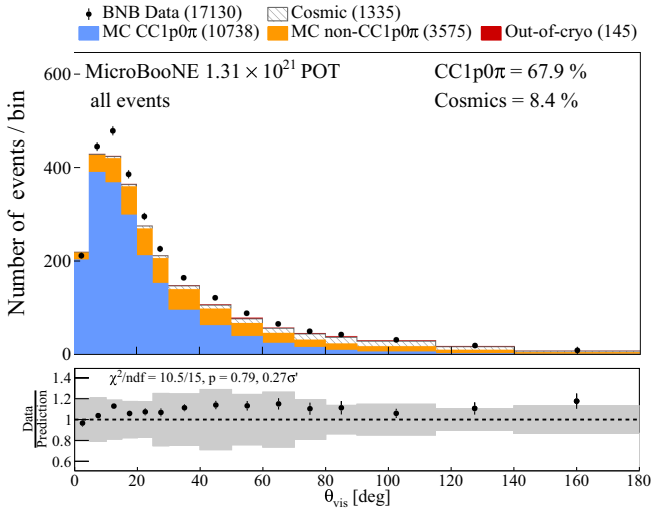


FIG. 3. Distribution of the selected CC1p0π events as a function of the angle θ_{vis}. Only statistical uncertainties are shown on the data. The bottom panel shows the ratio of data to prediction. The prediction uncertainty is included in the bottom panel. The data-simulation agreement is quantified across all the figures in terms of a goodness-of-fit metric (χ^2), the corresponding p-value (p), and as a number of standard deviations (σ').

background events as non-CC1p0π. In addition, there are also some remaining background contributions from cosmic contamination and interactions originating outside the cryostat.

The final θ_{vis} cross section results will be reported in regions of E_{reco}, p_n, and p_{miss}. These regions are listed in Table I and correspond to phase-space regions with sensitivity to different nuclear effects. The relevant event distributions in these regions are presented in Figs. 4–6. The θ_{vis} resolutions are included in the Supplemental Material [57]. The bin-width division has already been applied to account for the irregular binning. We further report the evolution of the θ_{vis} mean value (μ), standard deviation ($\tilde{\sigma}$), and median (m) in those regions for the simulated signal CC1p0π events. A representative example of the angular orientation θ_{vis} for the simulated signal CC1p0π events is presented as a function of the reconstructable energy in Fig. 7.

As can be seen both in Figs. 4–6 and in Table I, the median obtained in the θ_{vis} distribution using all the events (Fig. 3) is smaller than the median in regions with reconstructed energy less than 0.5 GeV shown in Fig. 4(a). The same behavior is observed for regions with high reconstructed struck nucleon momentum seen in Fig. 5(c) and regions with high missing momentum shown in Figs. 6(b) and 6(c). Yet, the resolutions obtained with the CC1p0π selection are, in most cases, smaller than the ones observed in the result reported in [63]. That

TABLE I. Evolution of the mean value (μ), standard deviation ($\tilde{\sigma}$), and median (m) as a function of θ_{vis} across various regions of E_{reco}, p_n, and p_{miss} for the simulated signal CC1p0π events.

Region	μ (deg)	$\tilde{\sigma}$ (deg)	m (deg)
All events	23.2	21.1	16.5
$E_{\text{reco}} < 0.5$ GeV	34.5	27.3	26.5
$0.5 < E_{\text{reco}} < 0.8$ GeV	21.8	18.6	16.5
$0.8 < E_{\text{reco}} < 2$ GeV	14.3	11.5	10.5
$p_n < 0.2$ GeV/c	10.0	5.8	9.5
$0.2 < p_n < 0.4$ GeV/c	21.8	11.4	19.5
$0.4 < p_n < 1$ GeV/c	49.3	26.3	44.5
$\lvert p_{\text{miss}}\rvert < 0.1$ GeV/c	20.7	19.4	15.5
$0.1 < \lvert p_{\text{miss}}\rvert < 0.2$ GeV/c	23.6	21.3	16.5
$0.2 < \lvert p_{\text{miss}}\rvert < 0.5$ GeV/c	29.8	23.6	23.5

observation is valid even at the lower part of the neutrino energy spectrum, where the reconstruction performance is expected to worsen.

IV. DUNE ATMOSPHERIC PROJECTION

In this section, we make a projection for the simulated θ_{vis} distribution expected for DUNE atmospheric searches using the ν_μ flux prediction from Honda *et al.* [64] at the Homestake site. This is motivated by the good agreement within uncertainties seen between data and prediction, which allows us to take advantage of our simulation dataset and make predictions for the expected angular resolution in DUNE. In order to make the DUNE projection, we use the probability distribution function (pdf) for the BNB and Honda ν_μ fluxes. As shown in Fig. 8(a) showing the flux pdfs, there is a significant overlap between the Honda flux and the low energy range of the BNB flux. Using the ratio between the two flux pdfs as a function of E_ν, we derive a reweighting function to transition between the two fluxes, as shown in Fig. 8(b).

This function is applied on an event-by-event basis on the simulated candidate CC1p0π events that satisfy the MicroBooNE BNB event selection outlined in Sec. III and are shown in Fig. 9(a). The reweighted distribution shown in Fig. 9(b) corresponds to the expected θ_{vis} behavior that DUNE atmospheric analyses might obtain when the Honda flux is used. The MicroBooNE detector properties and cross section modeling are assumed to be the same for the purpose of this DUNE reweighting study. As expected, due to the lower-energy Honda flux, the DUNE atmospheric distribution has a broader θ_{vis} distribution than the MicroBooNE BNB θ_{vis} one.

Figure 9 also includes the interaction contributions of the simulated candidate CC1p0π events for both the MicroBooNE result and the DUNE projection. Since the Honda flux peaks at lower energies compared to the BNB

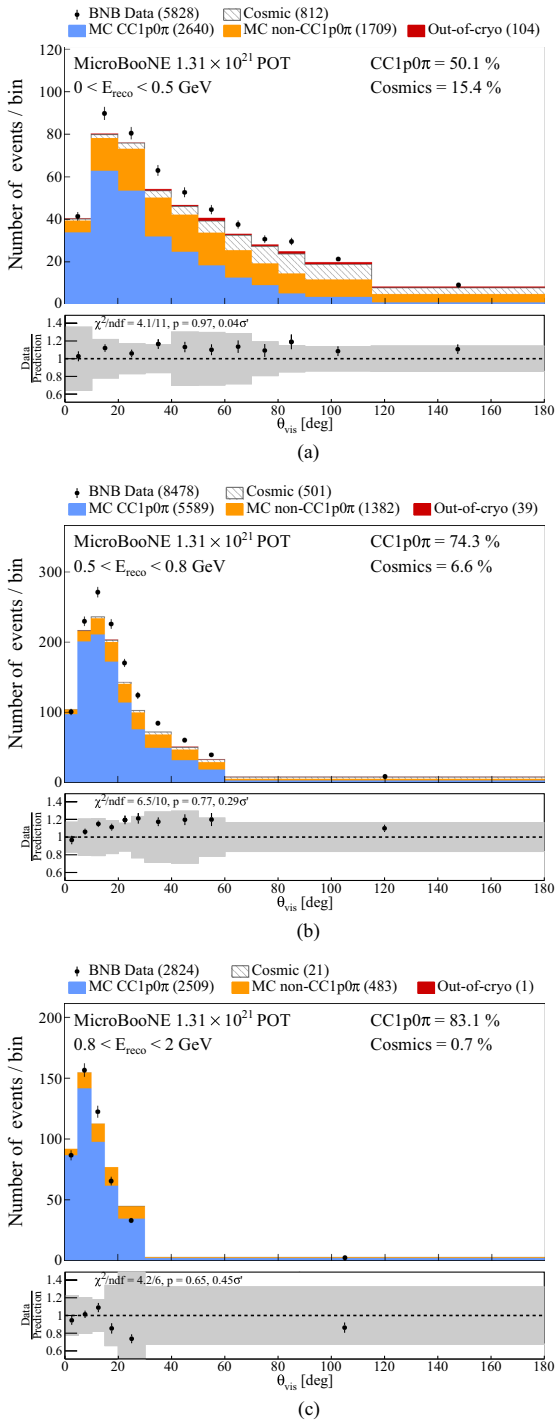


FIG. 4. Distribution of the selected CC1p0π events as a function of the muon-proton angle θ_{vis} in (a) low, (b) medium, and (c) high reconstructable energy (E_{reco}) regions. Only statistical uncertainties are shown on the data. The bottom panels show the ratio of data to prediction. The prediction uncertainty is included in the bottom panels. The data-simulation agreement is quantified across all the figures in terms of a goodness-of-fit metric (χ^2), the corresponding p-value (p), and as a number of standard deviations (σ').

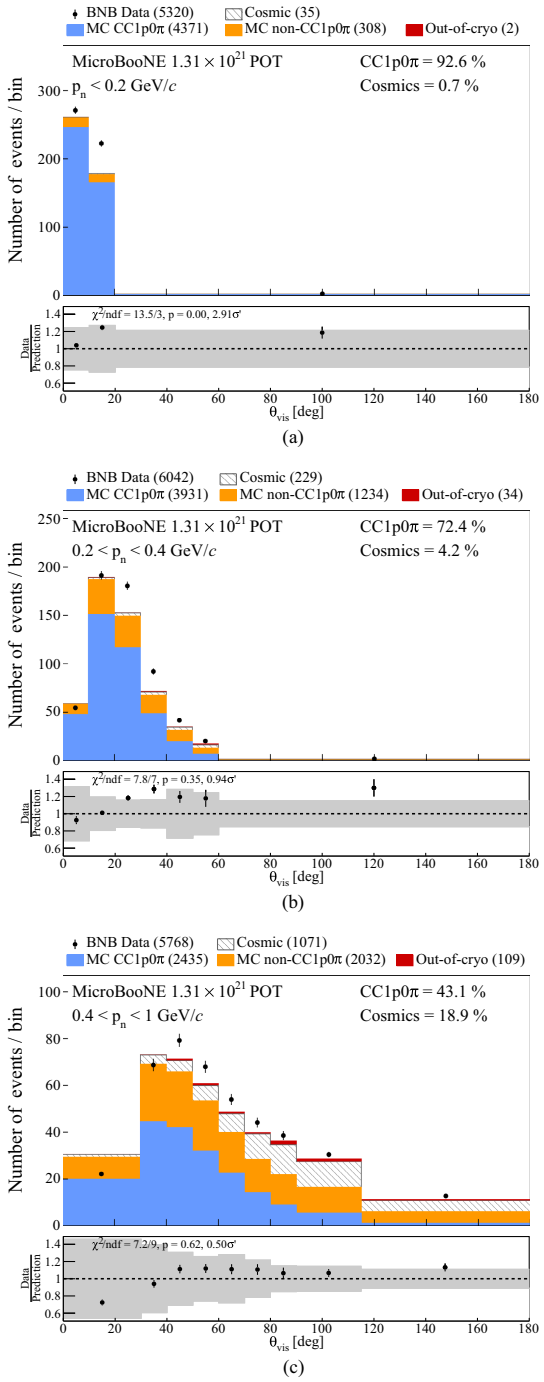


FIG. 5. Distribution of the selected CC1p0π events as a function of the muon-proton angle θ_{vis} in (a) low, (b) medium, and (c) high reconstructed struck nucleon momentum (p_n) regions. Only statistical uncertainties are shown on the data. The bottom panels show the ratio of data to prediction. The prediction uncertainty is included in the bottom panels. The data-simulation agreement is quantified across all the figures in terms of a goodness-of-fit metric (χ^2), the corresponding p-value (p), and as a number of standard deviations (σ').

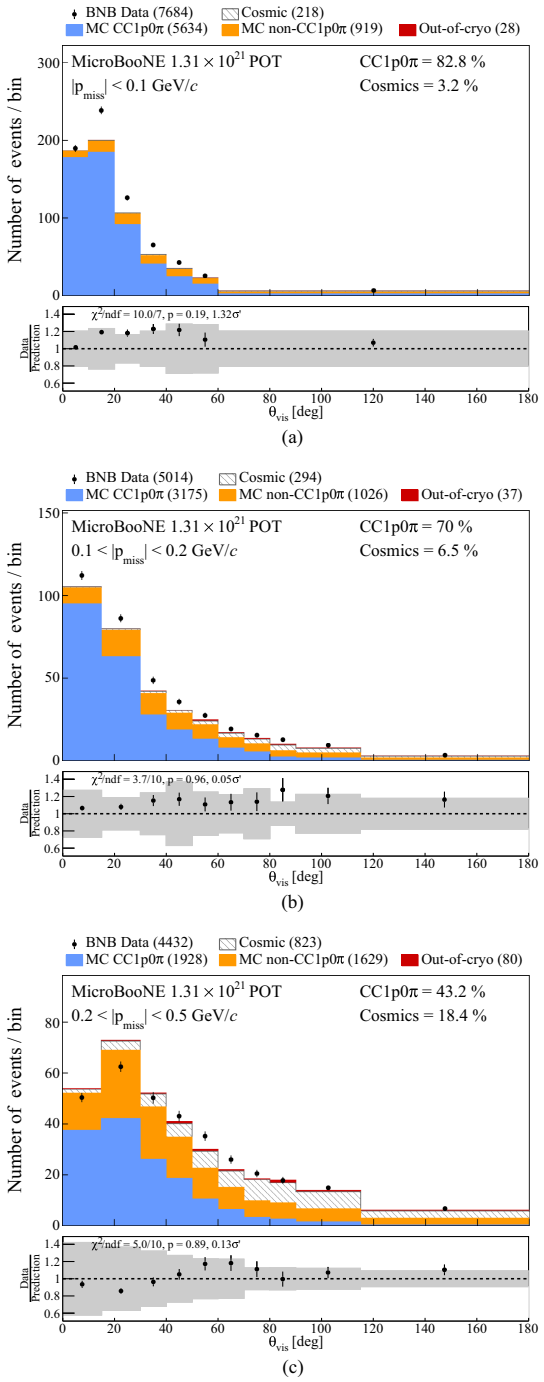


FIG. 6. Distribution of the selected CC1p0π events as a function of the muon-proton angle θ_{vis} in (a) low, (b) medium, and (c) high reconstructed missing momentum (p_{miss}) regions. Only statistical uncertainties are shown on the data. The bottom panels show the ratio of data to prediction. The prediction uncertainty is included in the bottom panels. The data-simulation agreement is quantified across all the figures in terms of a goodness-of-fit metric (χ^2), the corresponding p-value (p), and as a number of standard deviations (σ').

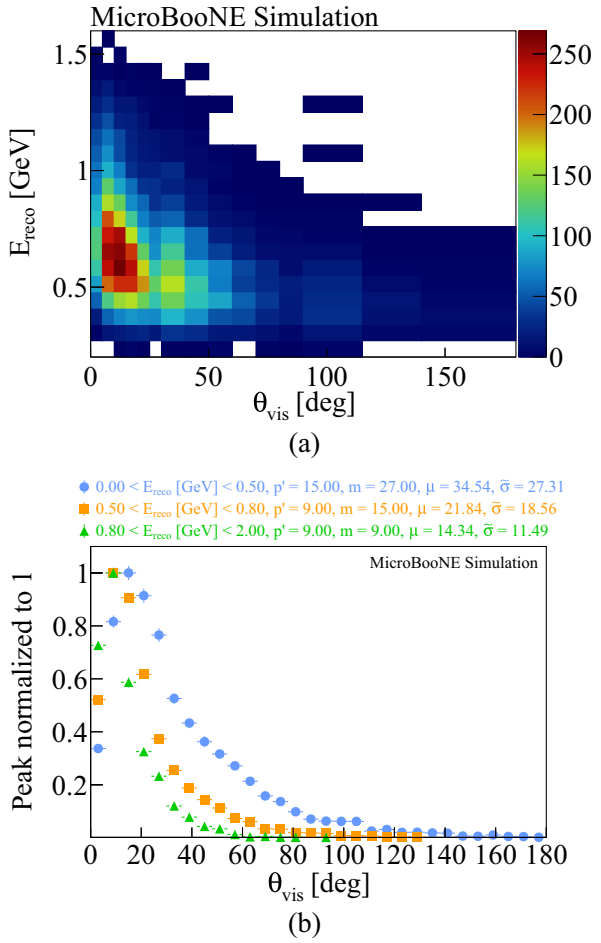


FIG. 7. (a) Angular orientation θ_{vis} dependence on the reconstructable energy using simulated signal CC1p0π events. (b) The θ_{vis} distributions presented in reconstructable energy slices using simulated signal CC1p0π events. The peak location (p'), median (m), mean value (μ), and standard deviation ($\tilde{\sigma}$) are also presented.

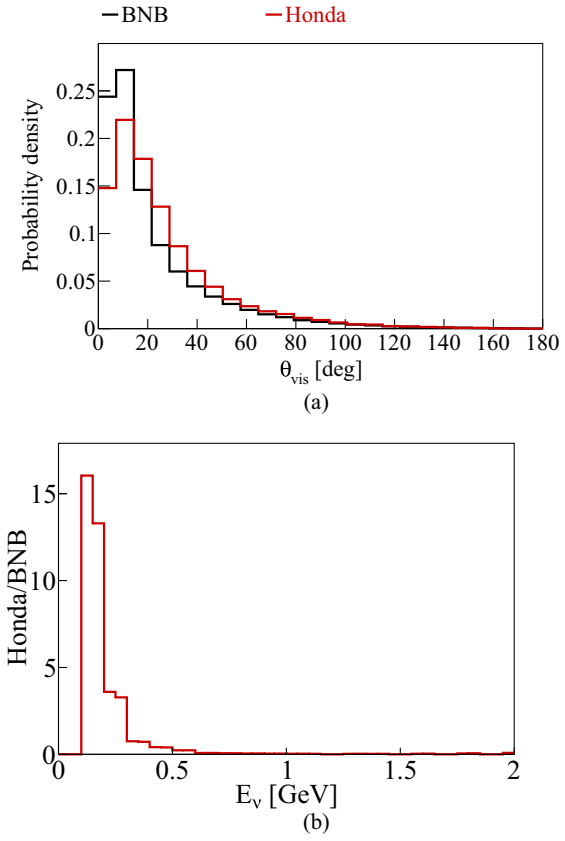


FIG. 8. (a) Comparison between the BNB and Honda ν_μ flux pdfs in true neutrino energy. (b) Reweighting function used for the BNB-to-Honda projection using the ratio of the ν_μ flux pdfs.

flux, the DUNE atmospheric projection has a higher contribution of QE events than MicroBooNE.

V. MICROBOONE CROSS SECTION MEASUREMENT

We report the extracted cross sections (σ) from the MicroBooNE data as a function of true kinematic variables using the Wiener singular value decomposition (Wiener-SVD) unfolding technique [65]. This technique transforms both the data measurement and covariance matrix into a regularized truth space. It requires the construction of a response matrix describing the expected detector smearing and reconstruction efficiency. This matrix is responsible for correcting for these effects. The input covariance matrix is constructed using the uncertainties related to the incident neutrino flux [30], interaction model [66], particle propagation [67], and detector response [68]. The binning is chosen to balance resolution and statistics. Each measurement is accompanied by an output regularization matrix A_C. The A_C matrix performs the conversion from the truth to the regularized truth space and is included in the Supplemental Material [57]. The unfolding is performed for each of the observables of interest using the `G18T` model described in Sec. III. The robustness of the unfolding method is verified using fake data studies with alternative generator predictions. Three fake data samples were investigating by (a) using NuWro v19.02.1 events [69], (b) removing the weights corresponding to the MicroBooNE tune from the default MC, and (c) multiplying the weight for the MEC events by a factor of two in the default MC.

The event rate has the predicted background subtracted before the unfolding. It is further divided by the integrated neutrino flux and number of argon nuclei in the fiducial volume to report a differential cross section. In the results presented in Figs. 10–15, the inner error bars on the cross sections correspond to the data statistical uncertainties. The systematic uncertainties are decomposed into data shape and normalization sources following the procedure outlined in Ref. [70]. The cross-term uncertainties are incorporated in the normalization. The outer error bars on the reported cross sections correspond to data statistical and shape uncertainties added in quadrature. The data normalization

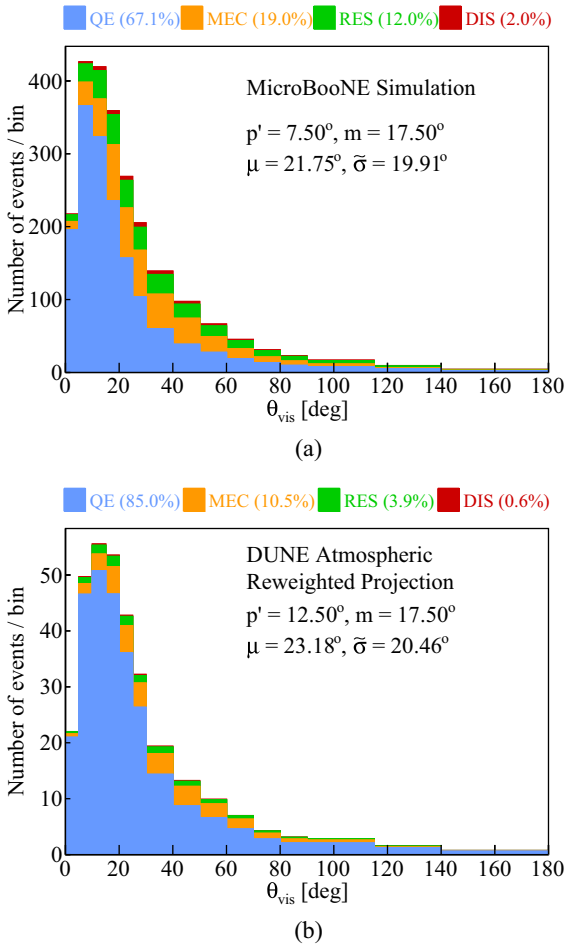


FIG. 9. Distribution of θ_{vis} using simulated candidate CC1p0π events for (a) MicroBooNE and (b) a DUNE atmospheric projection using the reweighting as a function of E_ν. The peak location (p'), median (m), mean value (μ), and standard deviation ($\tilde{\sigma}$) describing the distributions are also shown.

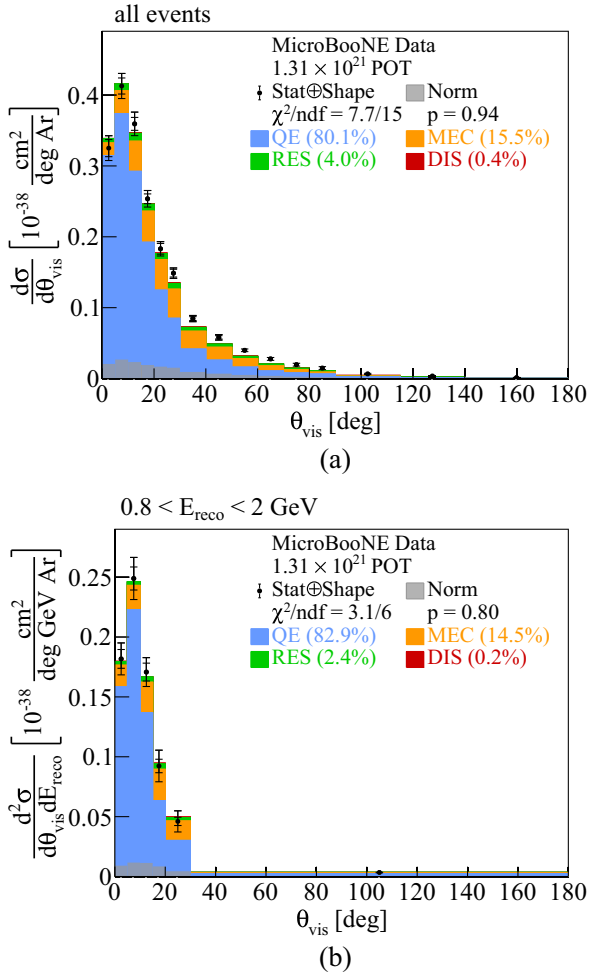


FIG. 10. (a) The unfolded cross section and the interaction contributions for the selected events for the `G18T` configuration as a function of θ_{vis}. (b) The unfolded cross section and the interaction contributions for the selected events using the same configuration as a function of θ_{vis} for events with $0.8 < E_{\text{reco}} < 2$ GeV. The gray band shows the normalization systematic uncertainty. Inner and outer error bars show the statistical and the statistical ⊕ shape uncertainty at the 1σ, or 68%, confidence level (CL).

uncertainties are presented as a band at the bottom of each plot. The degrees of freedom (d.o.f.) correspond to the number of bins. The χ^2/d.o.f. and p-value (p) data comparison for each generator prediction shown on all the figures takes into account the total covariance matrix. More details on the systematic uncertainties and the cross section extraction technique can be found in Ref. [32]. All the extracted cross sections are reported in the Supplemental Material [57]. They are compared to the `G18T` model set used by MicroBooNE, as well as the model set used by DUNE.

The single-differential cross section as a function of θ_{vis} is shown in Fig. 10(a). As expected from the reconstructed event spectrum shown in Fig. 3, it is a distribution that peaks at a nonzero value of ∼10° and extends to 180°. The low-θ_{vis} part of the distribution is dominated by QE interactions. The higher-θ_{vis} part of the spectrum has strong contributions from interactions with multinucleon effects, namely MEC and RES along with small DIS contributions. In this case where all events are considered, the `G18T` prediction yields good data-simulation agreement with a χ^2/d.o.f. less than one and a p-value close to unity.

As discussed in Sec. I, the neutrino angular orientation is of great importance for atmospheric neutrino oscillation studies. Thus, an extended θ_{vis} tail can be a limiting factor that introduces significant uncertainties and limits the experimental sensitivity. To that end, experimental efforts might want to primarily study events of interest in regions of the phase-space that result in a smaller spread of the θ_{vis} distribution. An example of such a phase-space region is shown in Fig. 10(b) and corresponds to higher reconstructable energies ($0.8 < E_{\text{reco}} < 2$ GeV) averaged over the relevant energy range. In this limited phase space, θ_{vis}

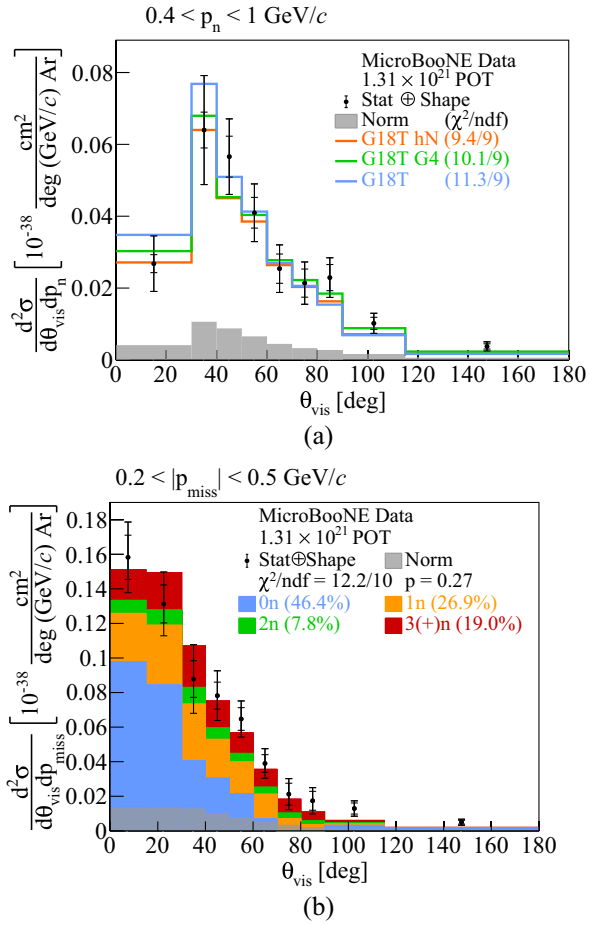


FIG. 11. (a) The flux-integrated double-differential cross sections as a function of θ_{vis} for $0.4 < p_n < 1$ GeV/c reported in regularized truth space. Colored lines show the results of theoretical cross section calculations using the `G18T hN` prediction with the hN FSI model (orange), the `G18T G4` prediction with the GEANT4 FSI model (green), and the `G18T` prediction with the hA FSI model (light blue). The gray band at the bottom shows the normalization systematic uncertainty. The numbers in parentheses show the χ^2/d.o.f. calculation for each of the predictions. (b) The flux-integrated double-differential cross sections as a function of θ_{vis} for $0.2 < |p_{\text{miss}}| < 0.5$ GeV/c reported in regularized truth space. Colored stacked histograms show the results of theoretical cross section calculations for events with no neutrons, `G18T 0n` (light blue), one neutron, `G18T 1n` (orange), two neutrons, `G18T 2n` (green), and at least three neutrons, `G18T 3(+)n` (red). The numbers in parentheses show the fractional contribution for each neutron multiplicity. Inner and outer error bars show the statistical and the statistical ⊕ shape uncertainty at the 1σ, or 68%, CL.

rarely exceeds 30° and the `G18T` prediction results in good agreement when compared to the data. Other phase space regions with small θ_{vis} spread are those with $p_n < 0.2$ GeV/c and $|p_{\text{miss}}| < 0.1$ GeV/c, as can be seen in Figs. 14 and 15, which will be shown later.

In contrast to these phase space restrictions that yield noticeably narrower θ_{vis} distributions, regions with a wide

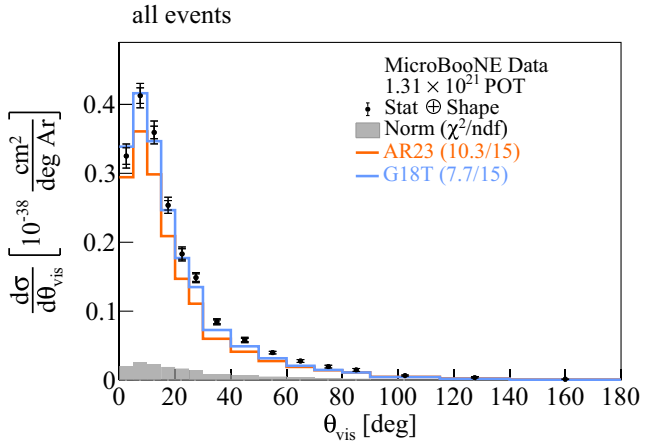
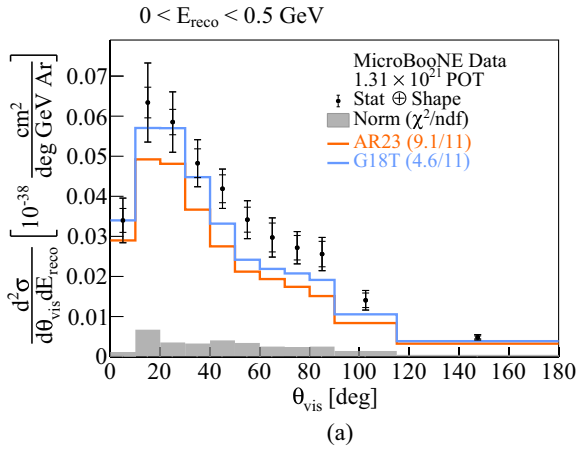
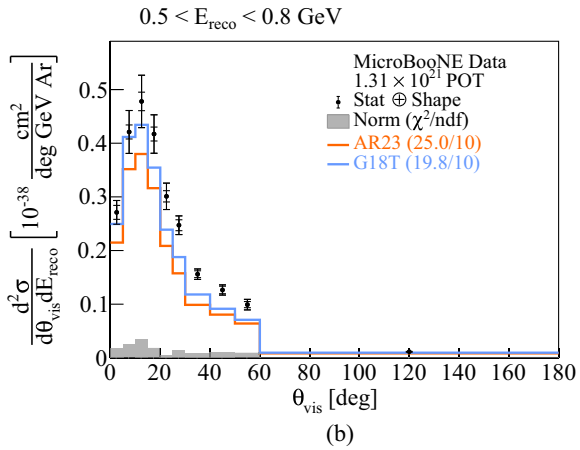


FIG. 12. The flux-integrated single-differential cross sections as a function of θ_{vis} reported in regularized truth space. The `G18T` (light blue) and `AR23` (orange) GENIE configuration predictions are compared to data. Inner and outer error bars show the statistical and the statistical ⊕ shape uncertainty at the 1σ, or 68%, CL. The gray band shows the normalization systematic uncertainty. The numbers in parentheses show the χ^2/d.o.f. calculation for each of the predictions.

angular spread have also been identified. Figure 11(a) shows an example corresponding to high total reconstructed struck nucleon momentum values ($0.4 < p_n < 1$ GeV/c). This phase space region has been shown to be dominated by events that undergo FSI [33]. To test the θ_{vis} FSI sensitivity in that region, we study the performance of different FSI modeling options using T2K-tuned GENIE configurations and compare them to the data results. These tuned configurations include the v3.0.6 `G18_10a_02_11` configuration with the empirical `hA2018` model (`G18T`) [50], the v3.0.6 `G18_10b_02_11` configuration with the `hN2018` cascade model (`G18b`) [71], and the v3.0.6 `G18_10d_02_11` configuration with the GEANT4-Bertini model (`G18d`) [72]. A comparison across the relevant predictions is shown in Fig. 11(a) and reveals that the three FSI models yield comparable predictions that describe the shape of the θ_{vis} distribution well. Discrimination power across the three FSI models could be established in future iterations of the analysis with reduced uncertainties in the first bins. A similar broadband θ_{vis} distribution is observed for low E_{reco} values and is presented in Fig. 13, which will be discussed later.

Other broad-spectrum features are observed for high missing momentum values ($0.2 < |p_{\text{miss}}| < 0.5$ GeV/c) in Fig. 11(b). The figure shows that these high missing momenta are obtained due to the presence of neutrons that deposit little to no energy in the detector, resulting in a tail that extends beyond 30° in θ_{vis}. Multineutron contributions account for more than half of the events in the high $|p_{\text{miss}}|$ sample. On the other hand, this reduces to 30% for events with low $|p_{\text{miss}}|$ values. The neutron contributions for the θ_{vis} distribution using all the selected events and those





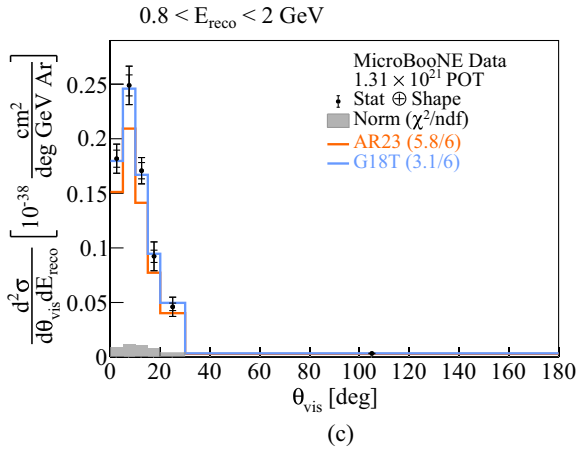
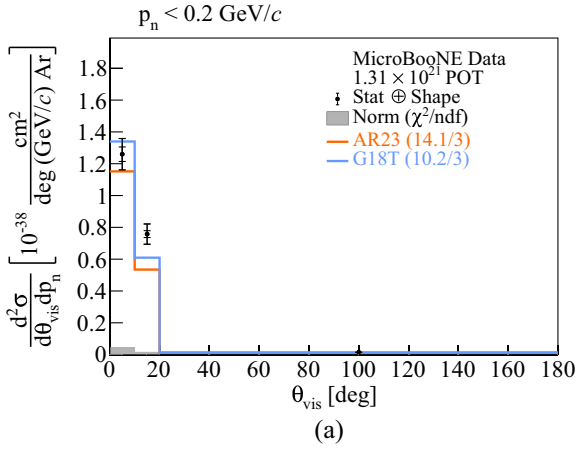
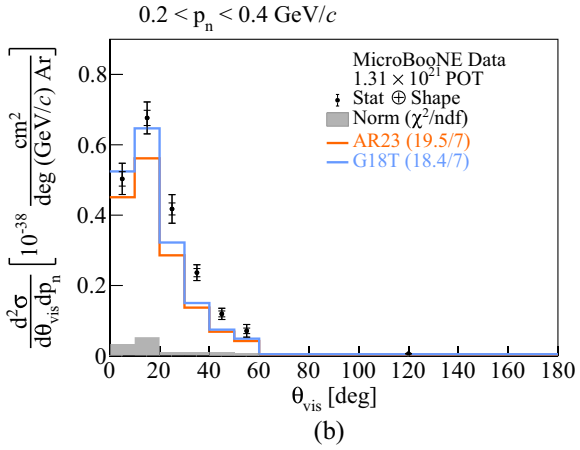


FIG. 13. The flux-integrated double-differential cross sections as a function of θ_{vis} for (a) $E_{\text{reco}} < 0.5$ GeV, (b) $0.5 < E_{\text{reco}} < 0.8$ GeV, and (c) $0.8 < E_{\text{reco}} < 2$ GeV. The G18T (light blue) and AR23 (orange) GENIE configuration predictions are compared to data. Inner and outer error bars show the statistical and the statistical ⊕ shape uncertainty at the 1σ, or 68%, CL. The gray band shows the normalization systematic uncertainty. The numbers in parentheses show the χ^2/d.o.f. calculation for each of the predictions.





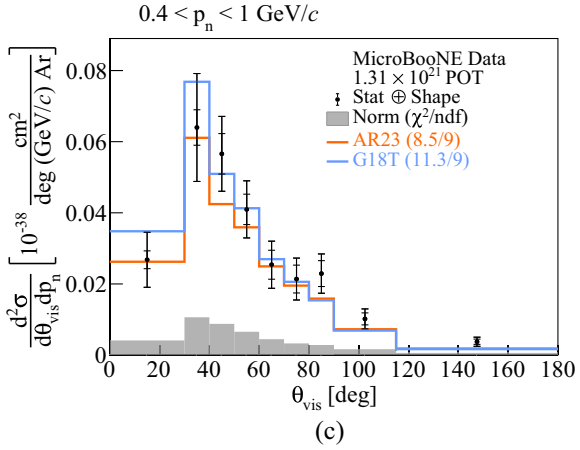


FIG. 14. The flux-integrated double-differential cross sections as a function of θ_{vis} for (a) $p_n < 0.2$ GeV/c, (b) $0.2 < p_n < 0.4$ GeV/c, and (c) $0.4 < p_n < 1$ GeV/c. The G18T (light blue) and AR23 (orange) GENIE configuration predictions are compared to data. Inner and outer error bars show the statistical and the statistical ⊕ shape uncertainty at the 1σ, or 68%, CL. The gray band shows the normalization systematic uncertainty. The numbers in parentheses show the χ^2/d.o.f. calculation for each of the predictions.

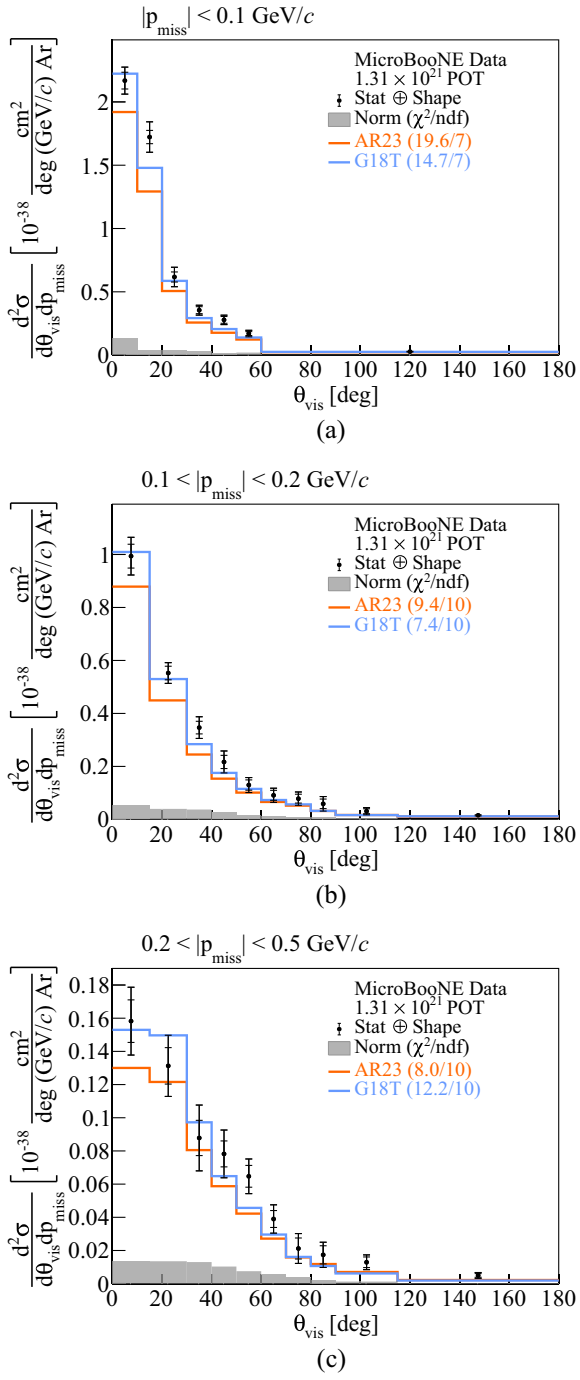


FIG. 15. The flux-integrated double-differential cross sections as a function of θ_{vis} for (a) $|p_{\text{miss}}| < 0.1$ GeV/c, (b) $0.1 < |p_{\text{miss}}| < 0.2$ GeV/c, and (c) $0.2 < |p_{\text{miss}}| < 0.5$ GeV/c. The G18T (light blue) and AR23 (orange) GENIE configuration predictions are compared to data. Inner and outer error bars show the statistical and the statistical ⊕ shape uncertainty at the 1σ, or 68%, CL. The gray band shows the normalization systematic uncertainty. The numbers in parentheses show the χ^2/d.o.f. calculation for each of the predictions.

events with $|p_{\text{miss}}| < 0.2$ GeV/c can be found in the Supplemental Material [57]. The importance of neutron detection in liquid argon has motivated a number of efforts and identification techniques [73–75].

For completeness, the data results are also compared against the `v3.4.2 GENIE AR23_20i_00_000` (AR23) model prediction that is currently used by DUNE and other Short-Baseline Neutrino (SBN) experiments. The AR23 model set shares many common features with the G18T one, but it includes some notable differences. Namely, AR23 uses the local Fermi gas ground state modeling along with a correlated high-momentum nucleon tail [38]; the z-expansion form factors for CCQE interactions [76]; the SuSAv2 modeling for MEC interactions [77]; emission of deexcitation photons for argon nuclei [38]; and the free nucleon tune [45].

Figure 12 shows the single-differential cross section measurement, while Figs. 13–15 show the double-differential cross sections as functions of θ_{vis} and E_{reco}, p_n and $|p_{\text{miss}}|$. AR23 yields a systematically lower prediction than G18T due to the fact that, unlike G18T, no tuning is applied on the AR23 QE contribution. Yet, there are also parts of the phase space where G18T demonstrates a poor performance with χ^2/d.o.f. greater than unity.

VI. CONCLUSIONS

We report on the precision of the reconstructed neutrino orientation θ_{vis} for event topologies with a single muon and a single proton in the final state. The data are recorded with the MicroBooNE LArTPC detector using the Booster Neutrino Beam at Fermi National Accelerator Laboratory with an exposure of 1.3×10^{21} protons on target. We find that the neutrino direction reconstruction performance using the single-proton selection is, in most cases, better than assumed in already published literature using an inclusive selection. Using a reweighting function in E_ν, we use the reconstructed simulated events in MicroBooNE to make a projection for the spectrum that the DUNE atmospheric studies might observe. The θ_{vis} cross sections are studied in phase-space regions of reconstructable neutrino energy, total struck nucleon momentum, and total missing momentum. The latter is agnostic to the angular orientation of the incoming neutrino and, therefore, can be used in atmospheric neutrino studies to separate events with better and worse directional reconstruction. The G18T modeling performance is found to be satisfactory within the extracted uncertainties and able to describe the majority of the nuclear effects driving the θ_{vis} distribution shape in different parts of the phase-space. We also report single-differential cross section measurements as a function of θ_{vis}, and double-differential cross section measurements as functions of θ_{vis} and the reconstructable visible energy, the total struck nucleon momentum, and the

missing momentum. These results can be used to inform the sub-GeV atmospheric oscillation studies that will be reported by forthcoming experiments like DUNE.

ACKNOWLEDGMENTS

This document was prepared by the MicroBooNE collaboration using the resources of the Fermi National Accelerator Laboratory (Fermilab), a U.S. Department of Energy, Office of Science, Office of High Energy Physics HEP User Facility. Fermilab is managed by Fermi Forward Discovery Group, LLC, acting under Contract No. 89243024CSC000002. MicroBooNE is supported by the following: the U.S. Department of Energy, Office of Science, Offices of High Energy Physics and Nuclear Physics; the U.S. National Science Foundation; the Swiss National Science Foundation; the Science and Technology Facilities Council (STFC), part of the United Kingdom Research and Innovation; the Royal Society (United Kingdom); the UK Research and Innovation (UKRI) Future Leaders Fellowship; and the NSF AI Institute for Artificial Intelligence and Fundamental Interactions. Additional support for the laser calibration system and cosmic ray tagger was provided by the Albert Einstein Center for Fundamental Physics, Bern, Switzerland. We also acknowledge the contributions of technical and scientific staff to the design, construction, and operation of the MicroBooNE detector as well as the contributions of past collaborators to the development of MicroBooNE analyses, without whom this work would not have been possible.

DATA AVAILABILITY

The data that support the findings of this article are openly available [78].

[1] K. Abe *et al.* (Super-Kamiokande Collaboration), Atmospheric neutrino oscillation analysis with external constraints in Super-Kamiokande I-IV, Phys. Rev. D **97**, 072001 (2018).
[2] M. G. Aartsen *et al.* (IceCube Collaboration), Measurement of atmospheric neutrino oscillations at 6–56 GeV with IceCube DeepCore, Phys. Rev. Lett. **120**, 071801 (2018).
[3] L. Wolfenstein, Neutrino oscillations in matter, Phys. Rev. D **17**, 2369 (1978).
[4] S. P. Mikheyev and A. Y. Smirnov, Resonance amplification of oscillations in matter and spectroscopy of solar neutrinos, Sov. J. Nucl. Phys. **42**, 913 (1985), https://inspirehep.net/literature/228623.
[5] E. K. Akhmedov, Neutrino oscillations in inhomogeneous matter (in Russian), Sov. J. Nucl. Phys. **47**, 301 (1988), https://inspirehep.net/literature/273549.
[6] P. Krastev and A. Smirnov, Parametric effects in neutrino oscillations, Phys. Lett. B **226**, 341 (1989).
[7] V. Barger, T. Weiler, and K. Whisnant, Generalized neutrino mixing from the atmospheric anomaly, Phys. Lett. B **440**, 1 (1998).
[8] A. Friedland, C. Lunardini, and M. Maltoni, Atmospheric neutrinos as probes of neutrino-matter interactions, Phys. Rev. D **70**, 111301 (2004).
[9] P. Huber, M. Maltoni, and T. Schwetz, Resolving parameter degeneracies in long-baseline experiments by atmospheric neutrino data, Phys. Rev. D **71**, 053006 (2005).
[10] E. K. Akhmedov, M. Maltoni, and A. Y. Smirnov, Neutrino oscillograms of the earth: Effects of 1-2 mixing and CP-violation, J. High Energy Phys. 06 (2008) 072.
[11] O. Mena, I. Mocioiu, and S. Razzaque, Neutrino mass hierarchy extraction using atmospheric neutrinos in ice, Phys. Rev. D **78**, 093003 (2008).
[12] O. L. G. Peres and A. Y. Smirnov, Oscillations of very low energy atmospheric neutrinos, Phys. Rev. D **79**, 113002 (2009).
[13] E. Fernandez-Martinez, G. Giordano, O. Mena, and I. Mocioiu, Atmospheric neutrinos in ice and measurement of neutrino oscillation parameters, Phys. Rev. D **82**, 093011 (2010).
[14] V. Barger, R. Gandhi, P. Ghoshal, S. Goswami, D. Marfatia, S. Prakash, S. K. Raut, and S. U. Sankar, Neutrino mass hierarchy and octant determination with atmospheric neutrinos, Phys. Rev. Lett. **109**, 091801 (2012).
[15] E. K. Akhmedov, S. Razzaque, and A. Y. Smirnov, Mass hierarchy, 2-3 mixing and CP-phase with huge atmospheric neutrino detectors, J. High Energy Phys. 02 (2013) 082.
[16] W. Winter, Neutrino mass hierarchy determination with IceCube-PINGU, Phys. Rev. D **88**, 013013 (2013).
[17] K. J. Kelly, P. A. N. Machado, N. Mishra, L. E. Strigari, and Y. Zhuang, Solar cycle effects in future measurements of low-energy atmospheric neutrinos, Phys. Rev. D **108**, 123019 (2023).
[18] Y. Zhuang, L. E. Strigari, and R. F. Lang, Time variation of the atmospheric neutrino flux at dark matter detectors, Phys. Rev. D **105**, 043001 (2022).
[19] C. A. Ternes, S. Gariazzo, R. Hajjar, O. Mena, M. Sorel, and M. Tórtola, Neutrino mass ordering at DUNE: An extra ν bonus, Phys. Rev. D **100**, 093004 (2019).
[20] P. B. Denton and R. Pestes, Neutrino oscillations through the Earth's core, Phys. Rev. D **104**, 113007 (2021).
[21] K. J. Kelly, P. A. N. Machado, I. Martinez-Soler, and Y. F. Perez-Gonzalez, DUNE atmospheric neutrinos: Earth tomography, J. High Energy Phys. 05 (2022) 187.
[22] C. A. Argüelles, P. Fernández, I. Martínez-Soler, and M. Jin, Measuring oscillations with a million atmospheric neutrinos, Phys. Rev. X **13**, 041055 (2023).

[23] K. J. Kelly, P. A. Machado, I. Martinez Soler, S. J. Parke, and Y. F. Perez Gonzalez, Sub-GeV atmospheric neutrinos and CP-violation in DUNE, Phys. Rev. Lett. **123**, 081801 (2019).
[24] B. Abi *et al.* (DUNE Collaboration), Long-baseline neutrino oscillation physics potential of the DUNE experiment, Eur. Phys. J. C **80**, 978 (2020).
[25] B. Abi *et al.* (DUNE Collaboration), Prospects for beyond the standard model physics searches at the deep underground neutrino experiment, Eur. Phys. J. C **81**, 322 (2021).
[26] B. Abi *et al.* (DUNE Collaboration), Supernova neutrino burst detection with the deep underground neutrino experiment, Eur. Phys. J. C **81**, 423 (2021).
[27] A. A. Abud *et al.* (DUNE Collaboration), Supernova pointing capabilities of DUNE, Phys. Rev. D **111**, 092006 (2025).
[28] O. Palamara, Exclusive muon neutrino charged current pion-less topologies. ArgoNeuT results and future prospects in LAr TPC detectors, in *Proceedings of the 10th International Workshop on Neutrino-Nucleus Interactions in Few-GeV Region (NuInt15)* (NuINT15, 2015), Chap. 10, p. 7566, 10.7566/JPSCP.12.010017.
[29] R. Acciarri *et al.* (MicroBooNE Collaboration), Design and construction of the MicroBooNE detector, J. Instrum. **12**, P02017 (2017).
[30] A. Aguilar-Arevalo *et al.* (MiniBooNE Collaboration), The neutrino flux prediction at MiniBooNE, Phys. Rev. D **79**, 072002 (2009).
[31] P. Abratenko *et al.* (MicroBooNE Collaboration), First double-differential measurement of kinematic imbalance in neutrino interactions with the MicroBooNE detector, Phys. Rev. Lett. **131**, 101802 (2023).
[32] P. Abratenko *et al.* (MicroBooNE Collaboration), Multi-differential cross section measurements of ν_μ-argon quasielasticlike reactions with the MicroBooNE detector, Phys. Rev. D **108**, 053002 (2023).
[33] P. Abratenko *et al.* (MicroBooNE Collaboration), Measurement of nuclear effects in neutrino-argon interactions using generalized kinematic imbalance variables with the MicroBooNE detector, Phys. Rev. D **109**, 092007 (2024).
[34] X. Lu and J. T. Sobczyk, Identification of nuclear effects in neutrino and antineutrino interactions on nuclei using generalized final-state correlations, Phys. Rev. C **99**, 055504 (2019).
[35] A. Bodek and T. Cai, Removal energies and final state interaction in lepton nucleus scattering, Eur. Phys. J. C **79**, 293 (2019).
[36] B. Bourguille, J. Nieves, and F. Sánchez, Inclusive and exclusive neutrino-nucleus cross sections and the reconstruction of the interaction kinematics, J. High Energy Phys. 04 (2021) 153.
[37] A. P. Furmanski and J. T. Sobczyk, Neutrino energy reconstruction from one-muon and one-proton events, Phys. Rev. C **95**, 065501 (2017).
[38] L. Alvarez-Ruso *et al.* (GENIE Collaboration), Recent highlights from GENIEv3, Eur. Phys. J. Special Topics **230**, 4449 (2021).
[39] R. Carrasco and E. Oset, Interaction of real photons with nuclei from 100-MeV to 500-MeV, Nucl. Phys. **A536**, 445 (1992).
[40] J. Nieves, F. Sanchez, I. Ruiz Simo, and M. Vicente Vacas, Neutrino energy reconstruction and the shape of the CCQE-like total cross section, Phys. Rev. D **85**, 113008 (2012).
[41] J. Engel, Approximate treatment of lepton distortion in charged current neutrino scattering from nuclei, Phys. Rev. C **57**, 2004 (1998).
[42] J. Nieves, J. E. Amaro, and M. Valverde, Inclusive quasielastic charged-current neutrino-nucleus reactions, Phys. Rev. C **70**, 055503 (2004).
[43] J. Schwehr, D. Cherdack, and R. Gran, GENIE implementation of IFIC Valencia model for QE-like 2p2h neutrino-nucleus cross section, arXiv:1601.02038.
[44] C. Berger and L. Sehgal, Lepton mass effects in single pion production by neutrinos, Phys. Rev. D **76**, 113004 (2007).
[45] J. Tena-Vidal *et al.* (GENIE Collaboration), Neutrino-nucleon cross-section model tuning in GENIEv3, Phys. Rev. D **104**, 072009 (2021).
[46] K. S. Kuzmin, V. V. Lyubushkin, and V. A. Naumov, Lepton polarization in neutrino–nucleon interactions, Mod. Phys. Lett. A **19**, 2815 (2004).
[47] C. Berger and L. Sehgal, PCAC and coherent pion production by low energy neutrinos, Phys. Rev. D **79**, 053003 (2009).
[48] U. K. Yang and A. Bodek, Parton distributions, d/u, and higher twist effects at high x, Phys. Rev. Lett. **82**, 2467 (1999).
[49] T. Sjöstrand, S. Mrenna, and P. Skands, PYTHIA6.4 physics and manual, J. High Energy Phys. 05 (2006) 026.
[50] D. Ashery, I. Navon, G. Azuelos, H. Walter, H. Pfeiffer, and F. Schleputz, True absorption and scattering of pions on nuclei, Phys. Rev. C **23**, 2173 (1981).
[51] K. Abe *et al.* (T2K Collaboration), Measurement of double-differential muon neutrino charged-current interactions on C_8H_8 without pions in the final state using the T2K off-axis beam, Phys. Rev. D **93**, 112012 (2016).
[52] P. Abratenko *et al.* (MicroBooNE Collaboration), New CC0π GENIE model tune for MicroBooNE, Phys. Rev. D **105**, 072001 (2022).
[53] C. Adams *et al.* (MicroBooNE Collaboration), Rejecting cosmic background for exclusive charged current quasi elastic neutrino interaction studies with liquid argon TPCs; a case study with the MicroBooNE detector, Eur. Phys. J. C **79**, 673 (2019).
[54] P. Abratenko *et al.* (MicroBooNE Collaboration), First measurement of differential charged current quasielasticlike ν_μ-argon scattering cross sections with the MicroBooNE detector, Phys. Rev. Lett. **125**, 201803 (2020).
[55] P. Abratenko *et al.* (MicroBooNE Collaboration), First measurement of energy-dependent inclusive muon neutrino charged-current cross sections on argon with the MicroBooNE detector, Phys. Rev. Lett. **128**, 151801 (2022).
[56] P. Abratenko *et al.* (MicroBooNE Collaboration), First measurement of inclusive electron-neutrino and antineutrino charged current differential cross sections in charged lepton energy on argon in MicroBooNE, Phys. Rev. D **105**, L051102 (2022).
[57] See Supplemental Material at http://link.aps.org/supplemental/10.1103/f8nt-ygng for the data release, the validation of the reweighting function, the fake data studies,

the covariance matrices, the regularization matrices, and the neutron breakdowns.

[58] A. A. Aguilar-Arevalo *et al.* (MiniBooNE Collaboration), First measurement of the muon antineutrino double-differential charged-current quasielastic cross section, Phys. Rev. D **88**, 032001 (2013).

[59] C. Andreopoulos *et al.*, The GENIE neutrino Monte Carlo generator, Nucl. Instrum. Methods Phys. Res., Sect. A **614**, 87 (2010).

[60] C. Andreopoulos *et al.*, The GENIE neutrino Monte Carlo generator: Physics and user manual, arXiv:1510.05494.

[61] P. Abratenko *et al.* (MicroBooNE Collaboration), Novel approach for evaluating detector-related uncertainties in a LArTPC using MicroBooNE data, Eur. Phys. J. C **82**, 454 (2022).

[62] J. Calcutt, C. Thorpe, K. Mahn, and L. Fields, GEANT4 reweight: A framework for evaluating and propagating hadronic interaction uncertainties in GEANT4, J. Instrum. **16**, P08042 (2021).

[63] J. Kopp, P. Machado, M. MacMahon, and I. Martinez-Soler, Improving neutrino energy reconstruction with machine learning, arXiv:2405.15867.

[64] M. Honda, M. S. Athar, T. Kajita, K. Kasahara, and S. Midorikawa, Atmospheric neutrino flux calculation using the NRLMSISE-00 atmospheric model, Phys. Rev. D **92**, 023004 (2015).

[65] W. Tang, X. Li, X. Qian, H. Wei, and C. Zhang, Data unfolding with Wiener-SVD method, J. Instrum. **12**, P10002 (2017).

[66] P. Abratenko *et al.* (MicroBooNE Collaboration), New CC0π GENIE model tune for MicroBooNE, Phys. Rev. D **105**, 072001 (2022).

[67] S. Agostinelli *et al.* (GEANT4 Collaboration), GEANT4–A simulation toolkit, Nucl. Instrum. Methods Phys. Res., Sect. A **506**, 250 (2003).

[68] P. Abratenko *et al.* (MicroBooNE Collaboration), Novel approach for evaluating detector-related uncertainties in a LArTPC using MicroBooNE data, Eur. Phys. J. C **82**, 454 (2022).

[69] T. Golan, J. Sobczyk, and J. Żmuda, Nuwro: The Wrocław Monte Carlo generator of neutrino interactions, Nucl. Phys. B, Proc. Suppl. **229–232**, 499 (2012), Neutrino 2010.

[70] K. Mahn, A search for muon neutrino and antineutrino disappearance in the booster neutrino beam, Ph.D. thesis, Columbia University, 2009.

[71] S. Dytman, Y. Hayato, R. Raboanary, J. T. Sobczyk, J. Tena-Vidal, and N. Vololoniaina, Comparison of validation methods of simulations for final state interactions in hadron production experiments, Phys. Rev. D **104**, 053006 (2021).

[72] D. H. Wright and M. H. Kelsey, The GEANT4 Bertini cascade, Nucl. Instrum. Methods Phys. Res., Sect. A **804**, 175 (2015).

[73] P. Abratenko *et al.* (MicroBooNE Collaboration), Demonstration of neutron identification in neutrino interactions in the MicroBooNE liquid argon time projection chamber, Eur. Phys. J. C **84**, 1052 (2024).

[74] S. Martynenko *et al.* (CAPTAIN Collaboration), Measurement of the neutron cross section on argon between 95 and 720 MeV, Phys. Rev. D **107**, 072009 (2023).

[75] D. O. Rivera, Neutron cross section measurement in the protoDUNE-SP experiment, Ph.D. thesis, University of Pennsylvania, 2023.

[76] A. S. Meyer, M. Betancourt, R. Gran, and R. J. Hill, Deuterium target data for precision neutrino-nucleus cross sections, Phys. Rev. D **93**, 113015 (2016).

[77] S. Dolan, G. D. Megias, and S. Bolognesi, Implementation of the SuSAv2-meson exchange current 1p1h and 2p2h models in GENIE and analysis of nuclear effects in T2K measurements, Phys. Rev. D **101**, 033003 (2020).

[78] MicroBooNE Collaboration, First study of neutrino angle reconstruction using quasielastic-like interactions in MicroBooNE, arXiv:2504.17758.